A novel somatosensory spatial navigation system outside the hippocampal formation

Xiaoyang Long and Sheng-Jia Zhang*

Department of Neurosurgery, Xinqiao Hospital, Army Medical University, Chongqing, China

*To whom correspondence should be addressed.

E-mail: sheng-jia.zhang@tmmu.edu.cn or sheng-jia.zhang@outlook.com

Summary

The hippocampal-parahippocampal formation has long been regarded as the only central site for the brain's spatial navigation system. Nevertheless, studies from patients with large medial temporal lobe lesions suggest that the hippocampal formation is not essential for space memory, indicating that spatial navigation might be computed with another still unknown representation system outside the medial temporal lobe structures. Such an extra-hippocampal navigational system has never been identified, however. Here we report the existence, in the rat somatosensory cortex only, of a novel "all-in-one" navigational system, which contains the full spectrum of all distinct spatial cell types including place, head-direction, border/boundary, conjunctive, speed and grid cells. All recorded somatosensory spatial cells, from freely behaving rats with microelectrodes, show similar firing characteristics to those detected previously in the hippocampal-parahippocampal structures. The somatosensory navigational system extends the classical theory of a cognitive map about space beyond two discrete hippocampal-entorhinal regions only into another single highly hierarchical neocortical domain, providing possible alternative and more sophisticated computational algorithms for spatial memory and cognitive mapping.

Introduction

Decades of research on the brain's spatial representation for position, orientation, border/boundary, speed and distance have intensively explored the hippocampal formation, revealing many functionally specialized yet different types of spatial cells, including place cells (O'Keefe and Dostrovsky, 1971), head-direction cells (Ranck, 1984; Taube et al., 1990), border/boundary vector cells (Lever et al., 2009; Solstad et al., 2008), speed cells (Kropff et al., 2015), conjunctive cells (Sargolini et al., 2006) and grid cells (Hafting et al., 2005). All of those distinct spatial cells were exclusively identified in the hippocampal-parahippocampal network including hippocampus, presubuculum, parasubiculum and medial entorhinal cortex (MEC) (Witter et al., 2014). It has been previewing that the brain's spatial navigational system is located extensively in the densely interconnected hippocampal formation (McNaughton et al., 2006).

However, spatial navigation cannot be discretely computed within the hippocampal-entorhinal loop and requires interacting networks of other brain regions or neocortical areas to incorporate multisensory information (Ekstrom and Ranganath, 2018; Poucet et al., 2015). On the one hand, growing evidence reveals that the brain's spatial navigation system is a highly dynamic and multimodal process and requires multiple cognitive processes such as attention, perception, sensory-motor integration, decision-making and goal-directed short-term memory (Aghajan et al., 2015; Ekstrom and Ranganath, 2018; Geva-Sagiv et al., 2015; Ravassard et al., 2013); on the other hand, continuous studies from patients with large medial temporal lobe (MTL) lesions indicate that both entorhinal cortex and hippocampus in human are not needed for spatial computation and navigation (Shrager et al., 2008; Squire and Wixted, 2011), calling into the question the central idea that the hippocampus and entorhinal cortex are the only locus for the brain's spatial navigational system (Moser et al., 2017). Instead, spatial cognition and computation might be accomplished either independently upstream of MTL or in parallel with an unknown brain region outside the hippocampal formation (Urgolites et al., 2016). However, such a novel spatial navigation system

encoding the full spectrum of all distinct spatial cell types has not been identified outside MTL so far.

The somatosensory input, besides visual, auditory or olfactory sensory input, plays a critical role in spatial navigation for rodent and human exploration (Geva-Sagiv et al., 2015; Gori et al., 2017； Ranganath, 2018). We therefore hypothesized that the somatosensory cortex might encode another independent or parallel spatial coordinate system, which should contain at least a few, if not all, of functionally specific spatial cell types similar to those previously identified in the hippocampal-entorhinal microcircuitry. To test this hypothesis, we recorded the spatial firing activity of the primary somatosensory cortex from freely moving rats with microelectrodes. Surprisingly, we identified all types of functionally specialized yet distinct spatial cells, which showed similar sensitivity to position, orientation, geometry, speed or distance within the single somatosensory cortex to those classical spatial cells discovered previously in the hippocampal-parahippocampal regions (Moser et al., 2017).

Results

Place cells in the somatosensory cortex

To explore whether the somatosensory cortex exhibits spatial firing characteristics, we implanted self-assembled microdrives (McNaughton et al., 1983) into the heads of 5 rats targeted for the rat primary somatosensory cortex. The Nissl-stained coronal brain sections confirmed the tetrode placements tracking through all six layers of the primary somatosensory cortex in recorded rats (**Fig. 1A** and **Fig. S1**). The neuronal activity of individual neurons was recorded with four tetrodes while rats moved freely and foraged randomly for food in a square or cylinder enclosure. Of all the well-separated somatosensory neurons, a large number of the recorded neurons showed apparent spatially selective firing patterns and had place-specific firing locations when rats randomly entered a particular field of the enclosure, the “place” field (O'Keefe and Dostrovsky, 1971). Since it is very difficult to penetrate and hold the tetrodes into the

superficial layers just below the dura during the chronic surgery, we were unable to record those neurons from superficial layer-I to layer-III. Almost all of the recorded neural activity was collected largely in layer-IV, layer-V and layer-VI within the rat primary somatosensory cortex. Neurons were classified as place cells if their spatial information score exceeded the 99th percentile in a randomly shuffled analysis across all of the recorded somatosensory neurons. 116 out of the 1385 recorded somatosensory neurons (8.4%) fulfilled this criteria, showed significant place-specific firing fields and were thus categorized as place cells (**Fig. 1B**). The average spatial information in bits per spike was 2.40 ± 0.06 (mean ± s.e.m.). This percentage is significantly higher than that of the entire shuffled population (**Fig. 1C**; $Z = 27.58$, $P < 0.001$; binomial test with expected P_0 of 0.01 among large samples). The average peak firing rate for the location-specific cells was 8.72 ± 0.70 Hz (mean ± s.e.m.). The areal distribution of various place firing fields relative to the field center was shown in **Fig. 1D**, with the average field size found to be 733.31 ± 42.6 cm^2 (mean ± s.e.m.). The histogram showed the distribution of the place firing field sizes from the classified somatosensory place cells (**Fig. 1E**). Notably, if we lowered the criteria to the 95th percentile usually used by others (Langston et al., 2010; Rubin et al., 2014; Wills et al., 2010), 342 out of the 1385 recorded somatosensory neurons (24.7%) fulfilled this less stringent criteria and were also classified as place cells, with the average spatial information score in bits per spike found to be 1.67 ± 0.04 (mean ± s.e.m.). We found no clear differences between classical hippocampal place cells and somatosensory place cells. Like those CA1 place cells from the hippocampus, somatosensory place cells traversed the entire available moving arena, and firing locations of individual place fields distributed uniformly in the two-dimensional open enclosure. Furthermore, we also detected many place cells with more than one field (**Fig. S2A**). Similar to those classical place cells recorded in the hippocampus, these somatosensory place cells were theta-modulated and also exhibit phase precession (**Fig. S3**) (O'Keefe and Recce, 1993).

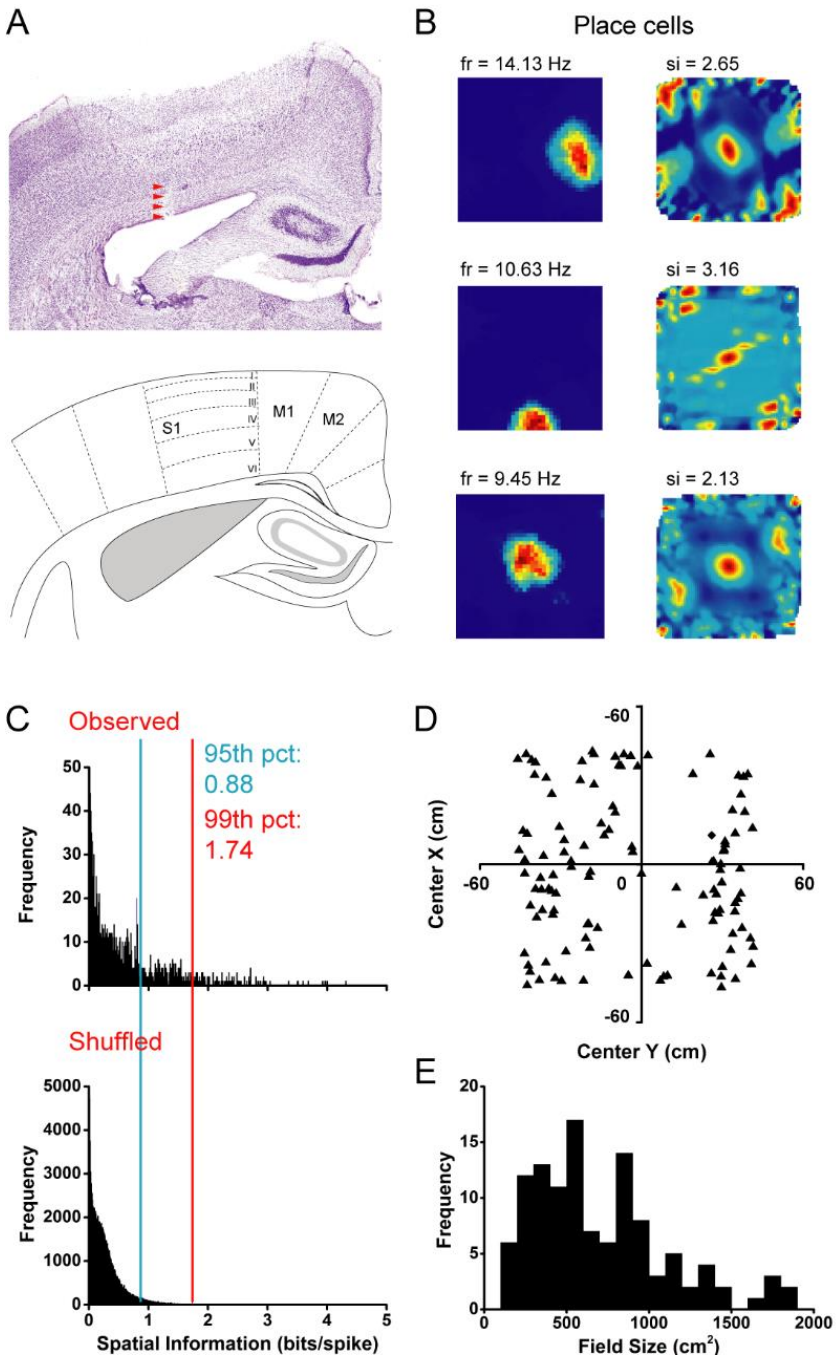

Fig. 1: Representative tetrode track and place cells in the somatosensory cortex.

(A) Nissl-stained coronal sections showing tetrode tracking trajectory (arrowheads) through all of six layers across the rat primary somatosensory cortex. (**B)** Heat maps of spatial firing rate (left column) and autocorrelation (right column) are color-coded with dark blue indicating minimal firing rate and dark red indicating maximal firing rate. The scale of the autocorrelation maps is twice that of the spatial firing rate maps. Maximal firing rate (fr) and spatial information (si) for each representative cell are

labelled at the top of the panels. (**C)** Distribution of spatial information for somatosensory cells. The top panel shows the distribution for observed spatial information. The bottom panel shows the distribution for randomly shuffled versions from the same sample. For each round of the shuffling process, the entire sequence of spike train from each cell was time-shifted along the animal's trajectory by a random interval between 20 s and trial duration minus 20 s, with the end wrapped around to the beginning of the trial, a spatial firing rate map was constructed, and spatial information was calculated. This shuffling process was repeated 100 times for each cell, generating a total of 138,500 permutations for the 1385 recorded somatosensory neurons. The red and blue stippled lines mark the 99th and the 95th percentile significance level of each randomly shuffled distribution, respectively. (**D**) The areal distribution of various place firing fields relative to the field center. (**E**) The histogram showed the distribution of the somatosensory place firing field sizes.

Head-direction cells in the somatosensory cortex

Head-direction cells discharge quickly only when the animal's head orientates to a particular angle (Taube et al., 1990). The animal's head direction was measured by tracking two different sizes of light-emitting diodes (LEDs), which were mounted to the heads of freely moving rats. To classify the directionality of each recorded cell, the mean vector length was used to compute head-direction tuning across 360 degrees (Rubin et al., 2014; Sargolini et al., 2006). Cells were categorized as direction-tuned if the mean vector length exceeded the 99th percentile of the total distribution of the shuffling procedure from the entire pool of recorded cells. 55 cells (4.0% of all recorded cells) met such criteria above, with the average length of the mean vector found to be 0.56 ± 0.02 (mean ± s.e.m.), showing significant modulation with the animal's head direction (**Fig. 2A**). This percentage is significantly higher than that of the entire shuffled population (**Fig. 2B**; $Z = 1.11$, $P < 0.001$). The average peak firing rate for the directionally modulated cells was 5.37 ± 0.61 Hz (mean ± s.e.m.). Notably, when we lowered the criteria to the 95th percentile usually used by others (Langston et al., 2010; Rubin et al., 2014; Wills et al., 2010), 185 out of the 1385 recorded somatosensory

neurons (13.4%) fulfilled this less stringent criteria and were then classified as head-direction cells, with the average length of the mean vector in bits per spike found to be 0.38 ± 0.01 (mean ± s.e.m.). The uniformity of distributed head-direction for all recorded directionally tuned cells was quantified with a $\chi 2$-test, and the preferred head-direction exhibited a uniform distribution (P = 0.60, **Fig. 2B** and **Fig. S4**). The head-direction modulation remained stable between the first and second halves of the recorded sessions. Strikingly, the primary somatosensory cortex now becomes the third extralimbic area besides the dorsal striatum and the medial precentral cortex, exhibiting the similar head-direction characteristics to those found previously within the limbic system (Laurens and Angelaki, 2018; Taube, 2007).

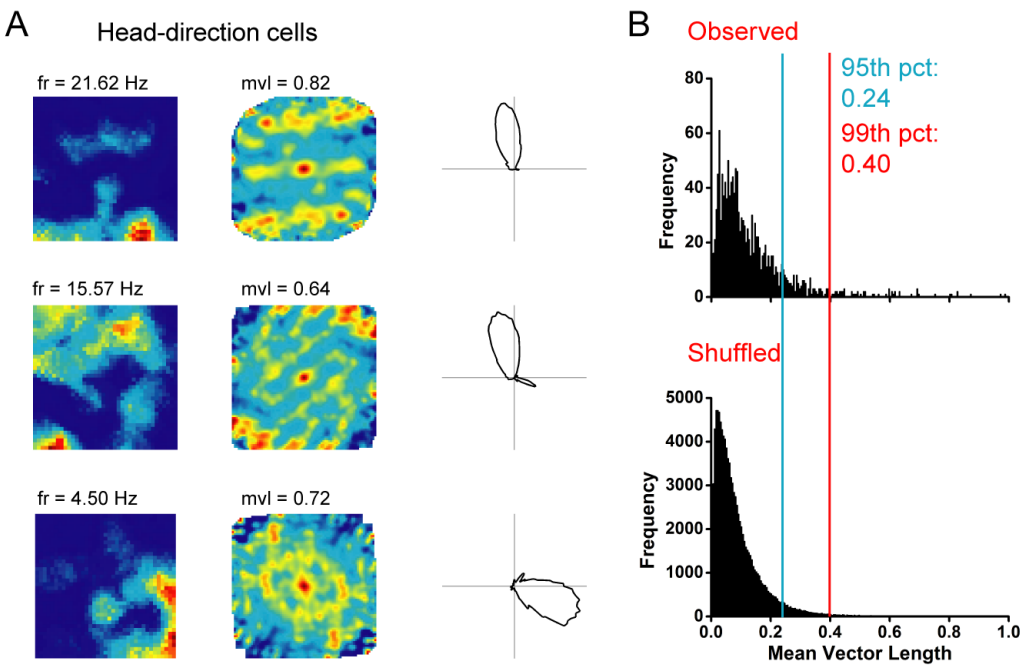

Fig. 2 Head-direction cells recorded from the somatosensory cortex.

(A) Three examples of somatosensory head-direction cells. Spatial firing rate maps (left column), autocorrelation diagrams (middle column) and head-direction tuning curves (right column). Firing rate is color-coded with dark blue indicating minimal firing rate and dark red indicating maximal firing rate. The scale of the autocorrelation maps is twice that of the spatial firing rate maps. Maximal firing rate (fr) and mean vector length (mvl) for each representative cell are labelled at the top of the panels. The directional

plots show strong head-direction tuning. (**B**) Distribution of mean vector length for somatosensory cells. The top panel shows the distribution for observed values. The bottom panel shows the distribution for randomly shuffled versions from the same sample. The red stippled lines mark the 99th and the 95th percentile significance level of each randomly shuffled distribution, respectively.

Border cells in the somatosensory cortex

We next examined whether the somatosensory cortex encodes border cells, which discharge exclusively whenever an animal is physically close to one or several environmental boundaries, for example the enclosure walls of the recording arena (Lever et al., 2009; Solstad et al., 2008). We then characterized border cells in the somatosensory cortex using the previous analysis approach (Solstad et al., 2008), in which the border score was calculated through dividing the sum of the maximal coverage of an individual wall over a single discharging field and the average distance of the fields from the adjacent wall by the difference between the two values above. Cells were defined as border cells if border scores were larger than the 99th percentile of those scores for shuffled data from all of the recorded somatosensory neurons (**Fig. 3A**). A total of 48 principal cells out of 1385 somatosensory cells (3.5%) were classified as border cells, and this percentage is significantly higher than that of the entire shuffled population (**Fig. 3B**; $Z = 9.22$, $P < 0.001$). Most cells fired along a single boundary while other cells had firing fields along two, three or even four boundaries within the running box (**Fig. 3A**). The average peak firing rate and the border score were 5.46 ± 0.80 Hz (mean ± s.e.m.) and 0.67 ± 0.01 (mean ± s.e.m.), respectively. Notably, once we lowered the criteria to the 95th percentile usually used by others (Langston et al., 2010; Rubin et al., 2014; Wills et al., 2010), 143 out of the 1385 recorded somatosensory neurons (10.3%) fulfilled this less stringent criteria and were then classified as border cells, with the average border score in bits per spike found to be 0.59 ± 0.01 (mean ± s.e.m.). Like those classical entorhinal border cells, somatosensory border cells produced a new yet parallel firing field along the wall of a discrete insert inside the square or cylinder enclosures (**Fig. S5**).

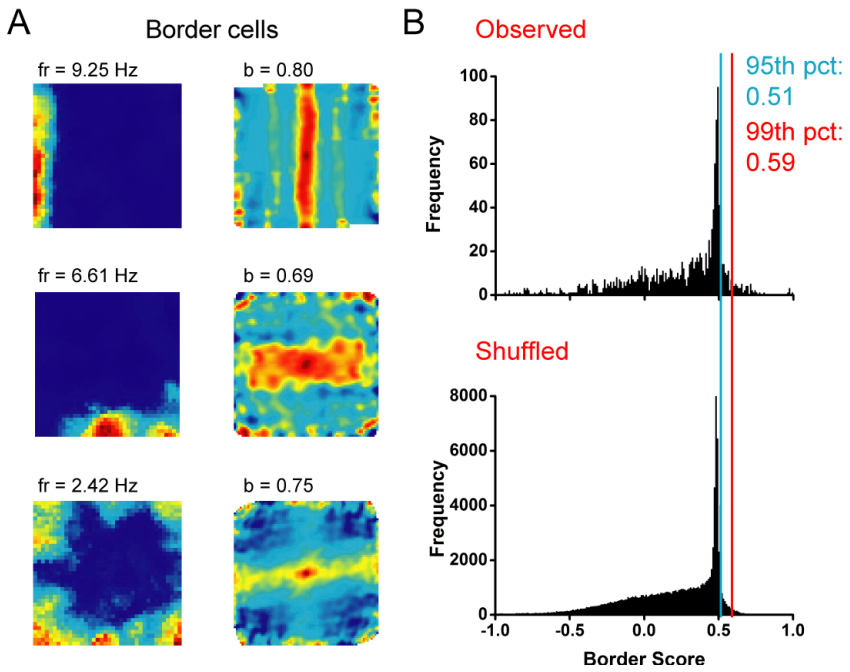

Fig. 3 Border cells recorded from the somatosensory cortex.

(A) Three representative examples of somatosensory border cells. Heat maps of spatial firing rate (left column) and autocorrelation diagrams (right column). Firing rate is color-coded with dark blue indicating minimal firing rate and dark red indicating maximal firing rate. The scale of the autocorrelation maps is twice that of the spatial firing rate maps. Maximal firing rate (fr) and border score (b) for each representative cell are labelled at the top of the panels. (**B**) Distribution of border scores for somatosensory cells. The top panel shows the distribution for observed values. The bottom panel shows the distribution for randomly shuffled versions from the same sample. The red and blue stippled lines mark the 99th and the 95th percentile significance level of each randomly shuffled distribution, respectively.

Grid cells in the somatosensory cortex

In the somatosensory cortex, we also observed the hexagonal firing patterns of grid cells similar to those identified in the MEC (Hafting et al., 2005). To quantify the regularity of hexagonal firing patterns of the somatosensory grid cells, we calculated grid scores of the entire population of recorded cells based on the Pearson correlation between the autocorrelogram of the firing field and its rotations (Langston et al., 2010;

Sargolini et al., 2006; Wills et al., 2010). A cell was categorized as a grid cell if its grid score was higher than the 99th percentile of the spatially shuffled data (**Fig. 4B**). 56 out of 1385 cells (4.0%) passed this criterion (**Fig. 4B**), and the fraction was significantly higher than that in the randomly shuffled data (Z = 11.92, P < 0.001). The average peak firing rate and the gridness score were 7.91 ± 1.04 Hz (mean ± s.e.m.) and 0.55 ± 0.02 (mean ± s.e.m.), respectively. The average grid space and gird field sizes were 41.30 ± 1.68 cm (mean ± s.e.m.) and 55.87 ± 2.86 cm (mean ± s.e.m.), respectively, with the grid orientation on the average found to be 39.12 ± 4.33 degree (mean ± s.e.m.) (**Fig. 4C, D**). Notably, while we lowered the criteria to the 95th percentile usually used by others (Langston et al., 2010; Rubin et al., 2014; Wills et al., 2010), 189 out of the 1385 recorded somatosensory neurons (13.6%) fulfilled this less stringent criteria and were then classified as grid cells, with the average gridness score in bits per spike to be 0.34 ± 0.01 (mean ± s.e.m.). The local configuration of grid cells in somatosensory cortex exhibited similar features as those in MEC, and we found most of somatosensory grid cells were also theta-modulated and exhibited phase precession (**Fig. S6A-C**). Strikingly, we detected a certain number of irregularly hexagonal patterns of grid cells with negative grid score from the somatosensory cortex, which were mixed with regular hexagonal patterns of the classical grid cells (**Fig. 4E and Fig. S4E)**. Furthermore, irregular somatosensory grid cells were also theta-modulated and showed phase precession (**Fig. S6D-F**). Such diverse repertoire of both irregular and regular hexagonal patterns of somatosensory grid cells co-exist in the same enclosure, indicating that the diverse patterns of both regular and irregular somatosensory gird cells might be internally created. Unlike the modular MEC grid cells, the intermingled somatosensory grid patterns might not be influenced by the environmental boundaries, pointing to possible overlapping yet different computational algorithms for spatial coding of genetically pre-configured ensembles of grid cells within the somatosensory cortex (Krupic et al., 2015; Stensola et al., 2015).

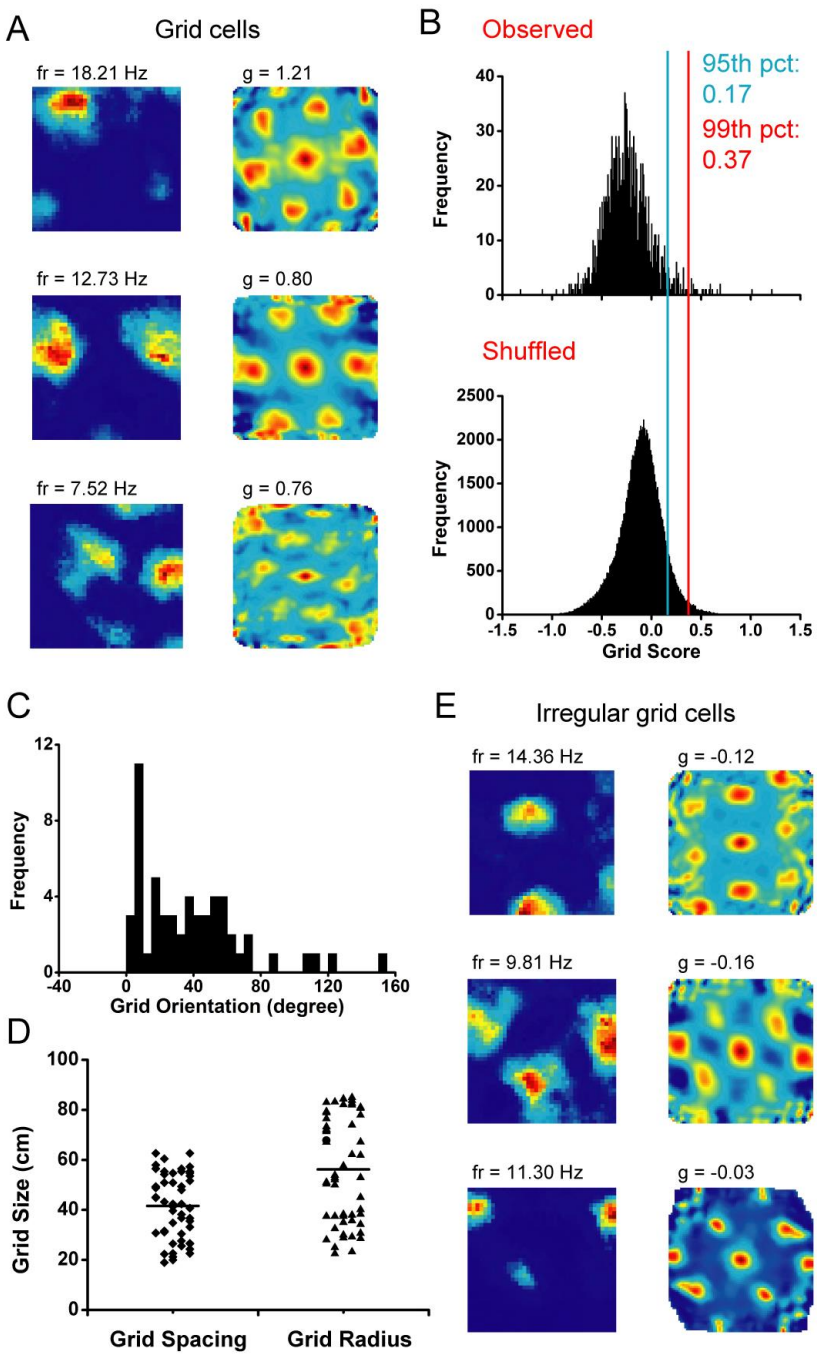

Fig. 4 Grid cells in the somatosensory cortex.

(A) Three representative examples of somatosensory grid cells. Heat maps of spatial firing rate (left column) and autocorrelation diagrams (right column). Firing rate is color-coded with dark blue indicating minimal firing rate and dark red indicating maximal firing rate. The scale of the autocorrelation maps is twice that of the spatial firing rate maps. Maximal firing rate (fr) and grid score (g) for each representative cell are labelled at the top of the panels. A crystal-like hexagonal firing patterns was

observed. (**B**) Distribution of grid scores for somatosensory cells. The top panel shows the distribution for observed values. The bottom panel shows the distribution for randomly shuffled versions from the same sample. The red and stippled lines mark the 99th and the 95th percentile significance level of each randomly shuffled distribution, respectively. (**C**) The frequency distribution of grid orientation from categorized somatosensory grid cells. (**D**) The raster plot showed the distribution of grid spacing and grid radius of the typical somatosensory grid cells. (**E**) Three representative examples of irregular somatosensory grid cells. Heat maps of spatial firing rate (left column) and autocorrelation diagrams (right column).

Conjunctive cells in the somatosensory cortex

To test whether somatosensory spatial cells encode conjunctive signals, we next assessed the head-directional tuning of all of the recorded somatosensory place cells, border cells and grid cells using the standard mean vector length (Rubin et al., 2014; Sargolini et al., 2006). A portion of the somatosensory spatial cells were conjunctive cells (**Fig. 5**), showing overlapping property of directionality with spatial information, border value or grid score. Altogether, 19 out of 116 place cells (**Fig. 5A**), 4 out of 48 border cells (**Fig. 5B**) and 3 out of 56 grid cells (**Fig. 5C**) were directionally tuned. Interestingly, we also detected irregular hexagonal grid cells modulated with head-direction (**Fig. 5D**). The degree of directionality in those cells showed no obvious difference from that of pure head-direction cells (mean U^2 values, 11.88 and 13.81, respectively; $P > 0.05$). These results suggest that the somatosensory cortex carries similar conjunctive spatial x directional, border x directional and gird x directional signal to those identified previously in the subiculum (Cacucci et al., 2004), MEC of rats (Sargolini et al., 2006; Solstad et al., 2008) and Egyptian fruit bats (Yartsev et al., 2011).

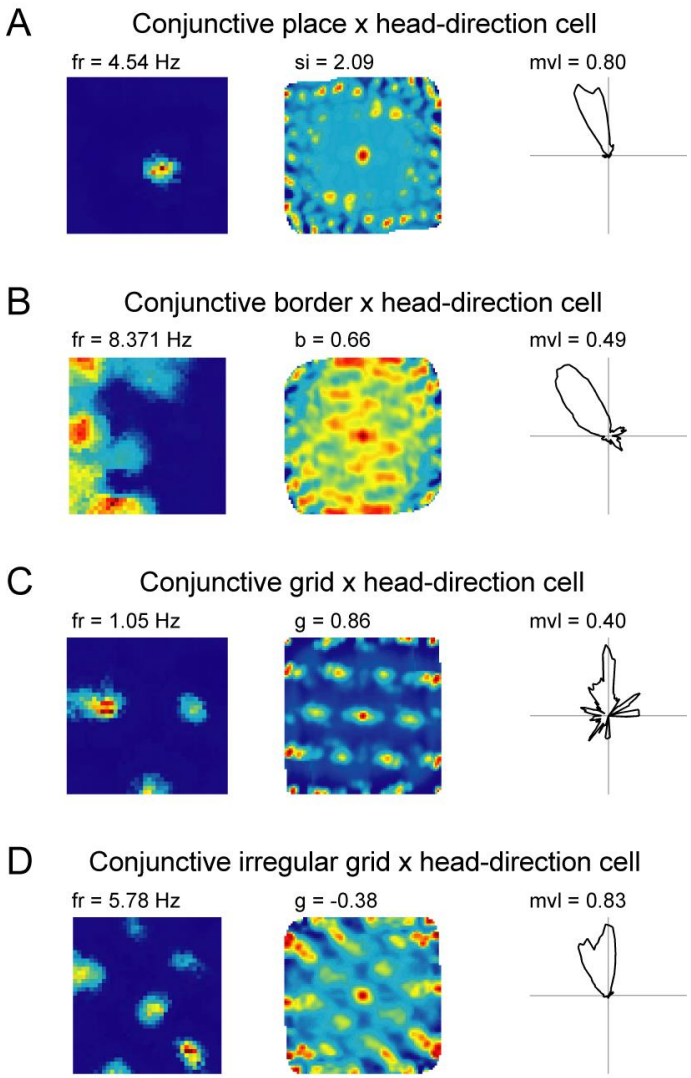

Fig. 5 Four different types of conjunctive cells in the somatosensory cortex.

(**A**) A representative conjunctive place x head directional cell. (**B**) A representative conjunctive border x head directional cell. (**C**) A representative conjunctive grid x head directional cell. (**D**) A representative conjunctive irregular grid x head directional cell. Spatial firing rate maps (left column), autocorrelation diagrams (middle column) and head-direction tuning curves (right column). Firing rate is color-coded with dark blue indicating minimal firing rate and dark red indicating maximal firing rate. The scale of the autocorrelation maps is twice that of the spatial firing rate maps. Maximal firing rate (fr), spatial information (si), border score (b), grid score (g) and mean vector length (mvl) for each representative cell are labelled at the top of the panels.

Discussion

The key finding of the present study is that we identified, for the first time to our knowledge, the full core of all different functionally specialized cell types for a previously undetected spatial representation system in the primary somatosensory cortex. The somatosensory navigational system contains similar place cells, head-direction cells, border cells, conjunctive cells and grid cells to those discovered previously in the classical hippocampal-parahippocampal formation (Burgess and O'Keefe, 2011; Moser et al., 2017). Strikingly, unlike the classical spatial navigation system which is confined to two anatomically discrete regions between hippocampus and MEC, this novel “all-in-one” somatosensory spatial navigational system is compactly assembled into a single brain area only but contains all of the building blocks for spatial memory and cognitive mapping. Notably, the somatosensory cortex, besides the dorsal striatum and the medial precentral cortex, now becomes the third extralimbic area and possesses similar head-direction signal to that identified with the rodent limbic system (Laurens and Angelaki, 2018; Taube, 2007).

Although few limited types of space-like cells were detected outside the hippocampal formation including the primary ferret auditory cortex (Town et al., 2017), the rat claustrum (Jankowski and O'Mara, 2015), the primary sensorimotor and premotor cortex in rhesus monkeys (Yin et al., 2018), the rat posterior parietal cortex (Wilber et al., 2014), the mouse retrosplenial cortex (Alexander and Nitz, 2015; Jacob et al., 2017; Mao et al., 2017; Whitlock et al., 2008), the rat septum (Leutgeb and Mizumori, 2002), the rat subiculum (Cacucci et al., 2004; Olson et al., 2017) and the primary rat visual cortex (Fiser et al., 2016), none of those brain regions above enabled encoding the full spectrum of such “all-in-one” spatial navigation system as the somatosensory cortex did.

We also detected a number of both fast-spiking interneurons and speed-responsive cells in the somatosensory cortex, in consistent with the earlier observation that the majority of hippocampal and entorhinal speed cells are fast-spiking GABAergic interneurons

(Hu et al., 2014; Kropff et al., 2015). Although we excluded both fast-spiking interneurons and speed cells in this study, how those somatosensory location-specific and direction-selective cell types are modulated with the somatosensory and/or hippocampal speed signals remains to be addressed (Ye et al., 2018).

This somatosensory spatial representation system has never been predicted with any classical theory for spatial learning and memory (McNaughton et al., 2006), although continuous studies of patients with large MTL lesions strongly argue against the central idea that the hippocampal-entorhinal network is the only site for encoding the brain's spatial navigation system (Shrager et al., 2008; Squire, 1992; Squire and Wixted, 2011). Our discovery of this single brain region-dependent somatosensory spatial representation system has implications for how hippocampal place fields and entorhinal grid patters are interacted (Frank et al., 2000). Currently, neither path integration-based attractor network model nor oscillatory interference model can explain well the formation of the hexagonal grid structures (Burgess and O'Keefe, 2011; Moser et al., 2014). Furthermore, previous developmental and lesion studies showed that hippocampal place cells mature earlier than entorhinal grid cells in developing rat puppies (Langston et al., 2010; Wills et al., 2010) and are not abolished by compromised grid input from lesioned MEC (Brandon et al., 2011; Koenig et al., 2011), contradicting the classical hypothesis that hippocampal place signals originate from MEC only (Burgess and O'Keefe, 2011).

Given only very sparse connections, if not none, between the somatosensory cortex and hippocampal formation (Cenquizca and Swanson, 2007; Insausti et al., 1997), whether the newly found somatosensory spatial navigation system is independent of, parallel with or convergent onto the classical one in the hippocampal-entorhinal microcircuit, how the place signals communicate with the grid cells within the somatosensory cortex, why the somatosensory grid modules are more diverse than the classical entorhinal grid patterns, what kinds of molecular and cellular triggers make such a pre-configured yet compact navigational system within the single somatosensory brain region during the

development of the central nervous system, and why the brain needs two anatomically discrete spatial representation systems are questions that will have to be studied, computationally and experimentally.

Since we do not know how much difference is between the coding principle of the somatosensory grid cells and that of the entorhinal grid cells, it remains to be revealed whether the somatosensory grid will be able to provide more efficient computational algorithms than the entorhinal grid for assembling computational architectures once adapted to deep learning-based artificial intelligence (Banino et al., 2018). However, given intermingled irregular and regular hexagonal patterns of grid cells within the somatosensory cortex, such single location-encoded spatial navigation system should provide much simplified yet more sophisticated computational algorithms for spatial coding and cortical computations. The availability of single-cell transcriptomics for both the somatosensory cortex and the MEC by *in situ* hybridization (Codeluppi et al., 2018; Ramsden et al., 2015), together with the reconstructed somatosensory microcircuit (Markram et al., 2015; Ramaswamy et al., 2015) and genetic tagging (Zhang et al., 2013), might help to unravel the molecular and cellular substrates of how two different grid maps are pre-configured genetically between these two distinct brain structures.

The somatosensory processing of the body motion information was found to link with the neural correlates of the spatial representation during an eight-arm maze task for rats (McNaughton et al., 1994), and a microcircuit theory of the somatosensory cortex has recently been proposed to be involved in body representation and body simulation (Brecht, 2017). It would therefore be interesting to find out whether motion-representation and self-representation share similar coding principle within the somatosensory cortex (Lisman et al., 2017). From a neural imaging and recording perspective, a much easier access to distinct spatial cells in the somatosensory cortex will facilitate how space memory is encoded, stored, consolidated, retrieved, and most importantly communicated among the hippocampal formation, the somatosensory

cortex and possibly other sensory-motor cortices (Campbell and Giocomo, 2018; Ekstrom and Ranganath, 2018; Ravassard et al., 2013; Wang and Morris, 2010). The newly detected somatosensory spatial representation system is likely to become a new framework and frontier in exploring episodic memory, spatial cognition and cortical computation as well as providing alternative therapeutic interventions for aging and neurodegenerative diseases.

References

1. Aghajan, Z.M., Acharya, L., Moore, J.J., Cushman, J.D., Vuong, C., and Mehta, M.R. (2015). Impaired spatial selectivity and intact phase precession in two-dimensional virtual reality. Nat Neurosci *18*, 121-128.
2. Alexander, A.S., and Nitz, D.A. (2015). Retrosplenial cortex maps the conjunction of internal and external spaces. Nat Neurosci *18*, 1143-1151.
3. Banino, A., Barry, C., Uria, B., Blundell, C., Lillicrap, T., Mirowski, P., Pritzel, A., Chadwick, M.J., Degris, T., Modayil, J., *et al.* (2018). Vector-based navigation using grid-like representations in artificial agents. Nature *557*, 429-433.
4. Brandon, M.P., Bogaard, A.R., Libby, C.P., Connerney, M.A., Gupta, K., and Hasselmo, M.E. (2011). Reduction of theta rhythm dissociates grid cell spatial periodicity from directional tuning. Science *332*, 595-599.
5. Brecht, M. (2017). The Body Model Theory of Somatosensory Cortex. Neuron *94*, 985-992.
6. Burgess, N., and O'Keefe, J. (2011). Models of place and grid cell firing and theta rhythmicity. Curr Opin Neurobiol *21*, 734-744.
7. Cacucci, F., Lever, C., Wills, T.J., Burgess, N., and O'Keefe, J. (2004). Theta-modulated place-by-direction cells in the hippocampal formation in the rat. J Neurosci *24*, 8265-8277.
8. Campbell, M.G., and Giocomo, L.M. (2018). Self-motion processing in visual and entorhinal cortices: inputs, integration, and implications for position coding. J Neurophysiol *120*, 2091-2106.
9. Cenquizca, L.A., and Swanson, L.W. (2007). Spatial organization of direct hippocampal field CA1 axonal projections to the rest of the cerebral cortex. Brain Res Rev *56*, 1-26.
10. Codeluppi, S., Borm, L.E., Zeisel, A., La Manno, G., van Lunteren, J.A., Svensson, C.I., and Linnarsson, S. (2018). Spatial organization of the somatosensory cortex revealed by osmFISH. Nat Methods *15*, 932-935.
11. Ekstrom, A.D., and Ranganath, C. (2018). Space, time, and episodic memory: The hippocampus is all over the cognitive map. Hippocampus *28*, 680-687.
12. Fiser, A., Mahringer, D., Oyibo, H.K., Petersen, A.V., Leinweber, M., and Keller, G.B. (2016). Experience-dependent spatial expectations in mouse visual cortex. Nat Neurosci *19*, 1658-1664.
13. Frank, L.M., Brown, E.N., and Wilson, M. (2000). Trajectory encoding in the hippocampus and entorhinal cortex. Neuron *27*, 169-178.
14. Geva-Sagiv, M., Las, L., Yovel, Y., and Ulanovsky, N. (2015). Spatial cognition in bats and

rats: from sensory acquisition to multiscale maps and navigation. Nat Rev Neurosci *16*, 94-108.

15. Gori, M., Cappagli, G., Baud-Bovy, G., and Finocchietti, S. (2017). Shape Perception and Navigation in Blind Adults. Front Psychol *8*, 10.

16. Hafting, T., Fyhn, M., Molden, S., Moser, M.B., and Moser, E.I. (2005). Microstructure of a spatial map in the entorhinal cortex. Nature *436*, 801-806.

17. Hu, H., Gan, J., and Jonas, P. (2014). Interneurons. Fast-spiking, parvalbumin(+) GABAergic interneurons: from cellular design to microcircuit function. Science *345*, 1255263.

18. Insausti, R., Herrero, M.T., and Witter, M.P. (1997). Entorhinal cortex of the rat: cytoarchitectonic subdivisions and the origin and distribution of cortical efferents. Hippocampus *7*, 146-183.

19. Jacob, P.Y., Casali, G., Spieser, L., Page, H., Overington, D., and Jeffery, K. (2017). An independent, landmark-dominated head-direction signal in dysgranular retrosplenial cortex. Nat Neurosci *20*, 173-175.

20. Jankowski, M.M., and O'Mara, S.M. (2015). Dynamics of place, boundary and object encoding in rat anterior claustrum. Front Behav Neurosci *9*, 250.

21. Koenig, J., Linder, A.N., Leutgeb, J.K., and Leutgeb, S. (2011). The spatial periodicity of grid cells is not sustained during reduced theta oscillations. Science *332*, 592-595.

22. Kropff, E., Carmichael, J.E., Moser, M.B., and Moser, E.I. (2015). Speed cells in the medial entorhinal cortex. Nature *523*, 419-424.

23. Krupic, J., Bauza, M., Burton, S., Barry, C., and O'Keefe, J. (2015). Grid cell symmetry is shaped by environmental geometry. Nature *518*, 232-235.

24. Langston, R.F., Ainge, J.A., Couey, J.J., Canto, C.B., Bjerknes, T.L., Witter, M.P., Moser, E.I., and Moser, M.B. (2010). Development of the spatial representation system in the rat. Science *328*, 1576-1580.

25. Laurens, J., and Angelaki, D.E. (2018). The Brain Compass: A Perspective on How Self-Motion Updates the Head Direction Cell Attractor. Neuron *97*, 275-289.

26. Leutgeb, S., and Mizumori, S.J. (2002). Context-specific spatial representations by lateral septal cells. Neuroscience *112*, 655-663.

27. Lever, C., Burton, S., Jeewajee, A., O'Keefe, J., and Burgess, N. (2009). Boundary vector cells in the subiculum of the hippocampal formation. J Neurosci *29*, 9771-9777.

28. Lisman, J., Buzsaki, G., Eichenbaum, H., Nadel, L., Ranganath, C., and Redish, A.D. (2017). Viewpoints: how the hippocampus contributes to memory, navigation and cognition. Nat Neurosci *20*, 1434-1447.

29. Mao, D., Kandler, S., McNaughton, B.L., and Bonin, V. (2017). Sparse orthogonal population representation of spatial context in the retrosplenial cortex. Nat Commun *8*, 243.

30. Markram, H., Muller, E., Ramaswamy, S., Reimann, M.W., Abdellah, M., Sanchez, C.A., Ailamaki, A., Alonso-Nanclares, L., Antille, N., Arsever, S., *et al.* (2015). Reconstruction and Simulation of Neocortical Microcircuitry. Cell *163*, 456-492.

31. McNaughton, B.L., Battaglia, F.P., Jensen, O., Moser, E.I., and Moser, M.B. (2006). Path integration and the neural basis of the 'cognitive map'. Nat Rev Neurosci *7*, 663-678.

32. McNaughton, B.L., Mizumori, S.J., Barnes, C.A., Leonard, B.J., Marquis, M., and Green, E.J. (1994). Cortical representation of motion during unrestrained spatial navigation in the rat. Cerebral cortex *4*, 27-39.

33. McNaughton, B.L., O'Keefe, J., and Barnes, C.A. (1983). The stereotrode: a new technique for simultaneous isolation of several single units in the central nervous system from multiple unit records. J Neurosci Methods *8*, 391-397.
34. Moser, E.I., Moser, M.B., and McNaughton, B.L. (2017). Spatial representation in the hippocampal formation: a history. Nat Neurosci *20*, 1448-1464.
35. Moser, E.I., Roudi, Y., Witter, M.P., Kentros, C., Bonhoeffer, T., and Moser, M.B. (2014). Grid cells and cortical representation. Nat Rev Neurosci *15*, 466-481.
36. O'Keefe, J., and Dostrovsky, J. (1971). The hippocampus as a spatial map. Preliminary evidence from unit activity in the freely-moving rat. Brain Res *34*, 171-175.
37. O'Keefe, J., and Recce, M.L. (1993). Phase relationship between hippocampal place units and the EEG theta rhythm. Hippocampus *3*, 317-330.
38. Olson, J.M., Tongprasearth, K., and Nitz, D.A. (2017). Subiculum neurons map the current axis of travel. Nat Neurosci *20*, 170-172.
39. Poucet, B., Chaillan, F., Truchet, B., Save, E., Sargolini, F., and Hok, V. (2015). Is there a pilot in the brain? Contribution of the self-positioning system to spatial navigation. Front Behav Neurosci *9*, 292.
40. Ramaswamy, S., Courcol, J.D., Abdellah, M., Adaszewski, S.R., Antille, N., Arsever, S., Atenekeng, G., Bilgili, A., Brukau, Y., Chalimourda, A., *et al.* (2015). The neocortical microcircuit collaboration portal: a resource for rat somatosensory cortex. Frontiers in neural circuits *9*, 44.
41. Ramsden, H.L., Surmeli, G., McDonagh, S.G., and Nolan, M.F. (2015). Laminar and dorsoventral molecular organization of the medial entorhinal cortex revealed by large-scale anatomical analysis of gene expression. PLoS Comput Biol *11*, e1004032.
42. Ranck, J.B.Jr. (1984). Head direction cells in the deep layer of dorsal presubiculum in freely moving rats. Soc. Neurosci. Abstr. 10:599.
43. Ravassard, P., Kees, A., Willers, B., Ho, D., Aharoni, D.A., Cushman, J., Aghajan, Z.M., and Mehta, M.R. (2013). Multisensory control of hippocampal spatiotemporal selectivity. Science *340*, 1342-1346.
44. Rubin, A., Yartsev, M.M., and Ulanovsky, N. (2014). Encoding of head direction by hippocampal place cells in bats. J Neurosci *34*, 1067-1080.
45. Sargolini, F., Fyhn, M., Hafting, T., McNaughton, B.L., Witter, M.P., Moser, M.B., and Moser, E.I. (2006). Conjunctive representation of position, direction, and velocity in entorhinal cortex. Science *312*, 758-762.
46. Shrager, Y., Kirwan, C.B., and Squire, L.R. (2008). Neural basis of the cognitive map: path integration does not require hippocampus or entorhinal cortex. Proc Natl Acad Sci U S A *105*, 12034-12038.
47. Solstad, T., Boccara, C.N., Kropff, E., Moser, M.B., and Moser, E.I. (2008). Representation of geometric borders in the entorhinal cortex. Science *322*, 1865-1868.
48. Squire, L.R. (1992). Memory and the hippocampus: a synthesis from findings with rats, monkeys, and humans. Psychol Rev *99*, 195-231.
49. Squire, L.R., and Wixted, J.T. (2011). The cognitive neuroscience of human memory since H.M. Annu Rev Neurosci *34*, 259-288.
50. Stensola, T., Stensola, H., Moser, M.B., and Moser, E.I. (2015). Shearing-induced asymmetry in entorhinal grid cells. Nature *518*, 207-212.

51. Taube, J.S. (2007). The head direction signal: origins and sensory-motor integration. Annu Rev Neurosci *30*, 181-207.
52. Taube, J.S., Muller, R.U., and Ranck, J.B., Jr. (1990). Head-direction cells recorded from the postsubiculum in freely moving rats. I. Description and quantitative analysis. J Neurosci *10*, 420-435.
53. Town, S.M., Brimijoin, W.O., and Bizley, J.K. (2017). Egocentric and allocentric representations in auditory cortex. PLoS Biol *15*, e2001878.
54. Urgolites, Z.J., Kim, S., Hopkins, R.O., and Squire, L.R. (2016). Map reading, navigating from maps, and the medial temporal lobe. Proc Natl Acad Sci U S A *113*, 14289-14293.
55. Wang, S.H., and Morris, R.G. (2010). Hippocampal-neocortical interactions in memory formation, consolidation, and reconsolidation. Annu Rev Psychol *61*, 49-79, C41-44.
56. Whitlock, J.R., Sutherland, R.J., Witter, M.P., Moser, M.B., and Moser, E.I. (2008). Navigating from hippocampus to parietal cortex. Proc Natl Acad Sci U S A *105*, 14755-14762.
57. Wilber, A.A., Clark, B.J., Forster, T.C., Tatsuno, M., and McNaughton, B.L. (2014). Interaction of egocentric and world-centered reference frames in the rat posterior parietal cortex. J Neurosci *34*, 5431-5446.
58. Wills, T.J., Cacucci, F., Burgess, N., and O'Keefe, J. (2010). Development of the hippocampal cognitive map in preweanling rats. Science *328*, 1573-1576.
59. Witter, M.P., Canto, C.B., Couey, J.J., Koganezawa, N., and O'Reilly, K.C. (2014). Architecture of spatial circuits in the hippocampal region. Philos Trans R Soc Lond B Biol Sci *369*, 20120515.
60. Yartsev, M.M., Witter, M.P., and Ulanovsky, N. (2011). Grid cells without theta oscillations in the entorhinal cortex of bats. Nature *479*, 103-107.
61. Ye, J., Witter, M.P., Moser, M.B., and Moser, E.I. (2018). Entorhinal fast-spiking speed cells project to the hippocampus. Proc Natl Acad Sci U S A *115*, E1627-E1636.
62. Yin, A., Tseng, P.H., Rajangam, S., Lebedev, M.A., and Nicolelis, M.A.L. (2018). Place Cell-Like Activity in the Primary Sensorimotor and Premotor Cortex During Monkey Whole-Body Navigation. Sci Rep *8*, 9184.
63. Zhang, S.J., Ye, J., Miao, C., Tsao, A., Cerniauskas, I., Ledergerber, D., Moser, M.B., and Moser, E.I. (2013). Optogenetic dissection of entorhinal-hippocampal functional connectivity. Science *340*, 1232627.

Materials and Methods

Subjects

5 male Long-Evans rats (2–4 months old, 250–450 grams at the time of the surgery) were used for this study. All animals were singly housed in transparent cages (35 cm×45 cm×45 cm, W×L×H) and maintained on a 12-hour reversed light-dark cycle (lights on from 9 p.m. to 9 a.m.). Experiments were performed during the dark phase. Rats were maintained in a vivarium with controlled temperature (19–22°C) and humidity (55–65%) near the recording room. The rats were kept at about 85-90% of free-feeding body weight and deprived of food 8–24 hours before each training and recording trial. Water was available *ad libitum*. All experiments were performed in accordance with the National Animal Welfare Act under a protocol approved by the Institute Animal Care and Use Committee.

Surgery and tetrode placement

The rats were anaesthetized first in the induction chamber with 5.0% isoflurane at an air-flow rate of 1400 ml/min and then with a mask under adjusted 0.5-3% isoflurane at an air-flow rate at 1000-1200 ml/min to appropriate physiological status during the surgery process. Microdrives loaded with four tetrodes were chronically implanted to the primary somatosensory cortex. Tetrodes were assembled with four twisted HM-L coated electrode wires, with a diameter of 17 µm and a composition of 90% platinum/10% iridium as well as with a diameter of 12.5 µm and a composition of 99.95% tungsten (California Fine Wire Company). The tip of each electrode made from platinum- or tungsten-coated wires was electroplated with platinum or gold, respectively to reduce its impedance to between 150 and 300 kΩ at 1 kHz with a computer-based nanoZ device (Chang et al., 2013). Coordinates for targeting to the rat primary somatosensory cortex were: anterior-posterior (AP): 0.2-2.2 mm posterior to bregma; medial-lateral (ML): 2.2-3.4 mm lateral to midline, dorsal-ventral (DV): 0.4/0.6-3 mm below the dura. 8-10 jeweler screws were attached into the rat skull, and individual microdrives were anchored to screws with several rounds of application of the dental cement. A jeweler's

screw was attached to the reference electrode to be used as a ground.

Training and data collection

Behavioral training, tetrode turning and data recording started one week post-surgery. The animals were trained to run around in a 1-m × 1-ms square box, and the two-dimensional opening enclosure is polarized by a white cue card. Running was motivated by randomly throwing crumbs of biscuit to the recording enclosure.

Each recording session lasted between 10 and 20 min. We lowered the depth-adjustable tetrodes with 50 μm increments until well-separated single units were identified. The recorded voltage signal was amplified by a factor of 5000-18,000, and the band-pass filter was set to 0.8-6.7 kHz. Threshold-triggered spikes were recorded at 48 kHz (50 samples per wave form, 8 bits per sample). The local field potential was recorded from one of the electrodes with a low-pass filter (500 Hz).

Spike sorting, cell classification and rate map

Spike sorting was manually performed offline with graphical cluster-cutting software (Tint, Axona Ltd, UK), and the clustering was primarily based on the spike waveform and the amplitude, together with additional autocorrelations and cross-correlations (Skaggs et al., 1996; Wilson and McNaughton, 1993). Two small light-emitting diodes (LEDs) were mounted to the headstage to track the animal's speed, position and orientation via an overhead a video camera. The animal's position was estimated based on dynamic tracking of the LEDs, which was linked to the headstage attached to the microdrive. Only spikes with instantaneous running speeds above 2.5 cm/s were chosen for further analysis.

To classify firing fields and firing rate distributions, the position data were divided into 2.5-cm × 2.5-cm bins, and the path was smoothed with a 21-sample boxcar window filter (400 ms; 10 samples on each side) (Boccara et al., 2010; Zhang et al., 2013). Maps for spike numbers and spike times were smoothed with a quasi-Gaussian kernel over

the neighboring 5 x 5 bins (Boccara et al., 2010; Langston et al., 2010; Zhang et al., 2013). Spatial firing rates were calculated by dividing the smoothed map of spike numbers with spike times. The peak firing rate was defined as the highest rate in the corresponding bin in the spatial firing rate map.

Analysis of place cells

Spatial information is a quantification of the extent to which a neuron's firing pattern can predict the position of freely moving animals and is expressed in the unit of bits per spike. The spatial information was calculated as:

$$\text{spatial information} = \sum_i p_i \frac{\lambda_i}{\lambda} \log_2 \frac{\lambda_i}{\lambda}$$

where λ_i is the mean firing rate of the cell in the *i*-th bin, λ is the overall mean firing rate of the cell in the trial, and p_i is the probability for the animal being at the location of the *i*-th bin. Adaptive smoothing (Skaggs et al., 1996) was applied to optimize the trade-off between spatial resolution and sampling error before the calculation of spatial information. The data were first divided into 2.5-cm × 2.5-cm bins, and then the firing rate within each bin was calculated by expanding a circle centered on the bin until

$$\gamma \geq \frac{\alpha}{n\sqrt{s}}$$

where γ is the circle's radius in bins, *n* is the number of occupancy of samples lying within the circle, *s* is the total number of spikes fired within the circle, and α is a constant parameter set to 10,000. With a position sampling frequency at 50 Hz, the firing rate assigned to that bin was then set to $50 \cdot s/n$.

The spatial correlation across trials from the same recording box was computed for each cell by correlating the firing rates in corresponding paired bins of two smoothed rate maps. The spatial stability within trials was estimated by calculating spatial correlations between firing rate maps generated from the first and second halves of the same trial.

A place cell was classified as a cell with the spatial information above the chance level,

which was computed by a random permutation process using all recorded cells. For each round of the shuffling process, the entire sequence of spike trains from each cell was time-shifted along the animal's trajectory by a random period between 20 s and the trial duration minus 20 s, with the end wrapped to the beginning of the trial. A spatial firing rate map was then constructed, and spatial information was calculated. This shuffling process was repeated 100 times for each cell, generating a total of 138,500 permutations for the 1385 somatosensory neurons. This shuffling procedure preserved the temporal firing characteristics in the unshuffled data while disrupting the spatial structure at the same time.

Spatial information score was then measured for each shuffled rate map. The distribution of spatial information values across all 100 permutations of all cells was computed and finally the 99th percentile of significant level was determined. The threshold values for categorizing cells into place cells were defined as the spatial information scores above the 99th percentile of the distribution from shuffled populations.

Analysis of grid cells

Spatial autocorrelation was calculated with smoothed spatial firing rate maps for all cells exceeding 100 spikes (Boccara et al., 2010; Sargolini et al., 2006; Zhang et al., 2013). Autocorrelograms were derived from Pearson's product moment correlation coefficient correcting for edge effects and unvisited locations.

With $\lambda(x,y)$ representing the average firing rate of a cell at coordinate (x,y), the autocorrelation between the spatial firing field itself and the spatial firing field with lags of τ_x and τ_y was calculated as:

$$\mathrm{r}(\tau_x,\tau_y) = \frac{\mathrm{n}\sum\lambda(x,y)\,\lambda\left(x-\tau_x,y-\tau_y\right)-\sum\lambda(x,y)\sum\lambda\left(x-\tau_x,y-\tau_y\right)}{\sqrt{n\sum\lambda(x,y)^2-[\sum\lambda(x,y)]^2}\sqrt{n\sum\lambda\left(x-\tau_x,y-\tau_y\right)^2-[\sum\lambda\left(x-\tau_x,y-\tau_y\right)]^2}}$$

where the summation is over whole n pixels in $\lambda(x,y)$ for which firing rate was

calculated for both $\lambda(x, y)$ and $\lambda(x - \tau_x, y - \tau_y)$. Autocorrelations were not calculated for spatial lags of τ_x, τ_y where $n < 20$.

The degree of spatial regularity ("gridness" or "grid score") was calculated for each recorded neuron by using a circular sample centered on the central peak of the autocorrelogram excluding the central peak itself, and by comparing rotated versions of this circular sample (Sargolini et al., 2006; Solstad et al., 2008). The Pearson's correlations between this circular sample and its rotated versions were calculated, with the angles of rotation of 60° and 120° in the first group, and 30°, 90° and 150° in the second group. Gridness or the neuron's grid score was defined as the minimal difference between any of the coefficients in the first group and any of the coefficients in the second group. Shuffling was performed in the same procedure used for defining place cells. Grid cells were categorized as cells with the rotational symmetry-based grid scores exceeding the 99th percentile of the distribution of grid scores for shuffled data from the entire population of somatosensory cells.

Grid spacing was computed as the median distance from the grid center to the closest peak among six neighboring firing fields in the autocorrelogram of the spatial firing map. Since such analysis is sensitive to noise in the grid autocorrelogram, grid spacing was computed only when the median distance to the six neighboring peaks for the analyzed cell was comparable to the radius of the circle centered on the gird autocorrelogram with the highest grid score. The radius of this circle around the center of the autocorrelogram was also referred to as the grid field size. When the ratio between grid spacing and grid field size was above 2 standard derivation (SD) of the mean value (mean ratio at 0.97, SD with 0.06), the cell was excluded (only 1 out of 56 cells had a noisy grid).

Grid orientation was calculated by first computing vectors from the center of the autocorrelogram to each of the three adjacent peaks among six neighboring firing fields in the autocorrelogram of the spatial firing map in the counterclockwise

direction, beginning with a camera-based reference line of zero degree. The angle between the minimal orientation of those three vectors and the camera-based reference line was defined as the grid orientation.

Analysis of head-direction cells

The animal's head directionality was estimated for each tracker sample by projecting the relative position of the two different sizes of LEDs onto the horizontal plane (Boccara et al., 2010; Langston et al., 2010; Sargolini et al., 2006; Zhang et al., 2013). The directional tuning curve for each recorded cell was drawn by plotting the spatial firing rate as a function of the rat's directionality, which is divided into bins of 3 degrees and then smoothed with a 14.5-degree mean window filter (2 bins on each side). In order to minimize the effect of inhomogeneous sampling on directionality estimates, sampling data were chosen only if all directional bins were occupied by the animal.

The strength of directionality was calculated by computing the mean vector length of the circular distribution of spatial firing rate. The chance values were determined by a shuffling process simulated in the same way as for place cells, with the entire sequence of spike trains time-shifted between 20 s and the whole trail length minus 20 s along the animal's trajectory. Cells were defined as head-direction cells if the mean vector lengths of the recorded cells were larger than the 99th percentile of the mean vector lengths in the shuffled distribution.

Analysis of border cells

Border or boundary vector cells were identified by calculating, for each recorded cell, the difference between the maximal length of any of the four walls touching on any single spatial firing field of the cell and the average distance of the firing field to the nearest wall, divided by the sum of those two values (Boccara et al., 2010; Solstad et al., 2008; Zhang et al., 2013). Border scores ranged from −1 for cells with perfect central firing fields to +1 for cells with firing fields that exactly line up with at least one entire wall. Firing fields were defined as summation of neighboring pixels with total

firing rates higher than 0.3 times the cell's maximum firing rate that covered a total area of at least 200 cm^2.

Border cells were classified as cells with border scores significantly higher than the degree of wall-relevant firing that would be expected for somatosensory cells by chance. The significance level was calculated by a shuffling process performed for experiments in the square enclosures in the same way as for place cells, head-direction cells and grid cells. For each permutation trial, the whole sequence of spike trains was time-shifted along the animal's trajectory by a random period between 20 s and 20 s less than the length of the entire trial, with the end wrapped to the start of the trial. A spatial firing rate map was then obtained, and a border score was estimated.

The distribution of border scores was calculated for the entire set of permutation trials from all recorded cells, and the 99th percentile was then determined. Cells were defined as border cells if the border score from the observed data was higher than the 99th percentile for border scores in the entire distribution generated from the permutated data.

Analysis of theta modulation and phase precession

To calculate fluctuations of neural activity through the theta cycle, we offline-filtered local electroencephalography (EEG) signals according to the approach taken previously (Langston et al., 2010). For the low-pass filtering, 4 and 5 Hz were selected as stopband and passband low cut-off frequencies, respectively, while 10 and 11 Hz were selected as passband and stopband high cut-off frequencies, respectively. Every spike from single-unit waveform clusters was assigned a phase in relation to the filtered theta signal, with 0 degree and 180 degree defined as the peak and the trough of the filtered signal, respectively. Clustering of firing phases within the entire theta cycle was calculated with Rayleigh's test to evaluate the uniformity of circular distributions. The cell's degree of phase precession was fitted with a linear regression line, the significance of the phase precession was estimated with the *F*-test. Theta modulation of single-unit

waveform clusters was calculated from the fast Fourier transform (FFT)-based power spectrum of the spike-train autocorrelation. When the mean spectral power within 1 Hz range of the theta peak within the 4-11 Hz frequency range was at least 3 times larger than the mean spectral power from 0 Hz to 125 Hz, the cell was defined as theta modulated.

Histology and reconstruction of recording positions

At the end of the recording sessions, the rats were anesthetized with overdose of sodium pentobarbital and perfused transcardially with phosphate-buffered saline (PBS) followed by 4% paraformaldehyde (PFA). Brains were removed and stored in 4% PFA overnight. The brain was then placed in 10, 20 and 30% sucrose/PFA solution sequentially for 24 h at each sucrose solution before sectioning by a cryostat microtome. All coronal sections around the tetrode tracking were collected and sliced into 30 µm. Sections were mounted on glass slides and stained with cresyl violet (Sigma-Aldrich) for Nissl body. The tetrode recording positions were determined from digitized images of the Nissl-staining sections. All electrode traces were confirmed to be located within the primary somatosensory cortex, based on The Rat Brain by Paxions & Watson (Paxinos and Watson, 2007).

Supporting References (S1-S9)

1. Boccara, C.N., Sargolini, F., Thoresen, V.H., Solstad, T., Witter, M.P., Moser, E.I., and Moser, M.B. (2010). Grid cells in pre- and parasubiculum. Nat Neurosci *13*, 987-994.
2. Chang, E.H., Frattini, S.A., Robbiati, S., and Huerta, P.T. (2013). Construction of microdrive arrays for chronic neural recordings in awake behaving mice. J Vis Exp, e50470.
3. Langston, R.F., Ainge, J.A., Couey, J.J., Canto, C.B., Bjerknes, T.L., Witter, M.P., Moser, E.I., and Moser, M.B. (2010). Development of the spatial representation system in the rat. Science *328*, 1576-1580.
4. Paxinos, G., and Watson, C. (2007). The rat brain in stereotaxic coordinates, Vol 552 (Amsterdam: Elsevier).
5. Sargolini, F., Fyhn, M., Hafting, T., McNaughton, B.L., Witter, M.P., Moser, M.B., and Moser, E.I. (2006). Conjunctive representation of position, direction, and velocity in entorhinal cortex. Science *312*, 758-762.
6. Skaggs, W.E., McNaughton, B.L., Wilson, M.A., and Barnes, C.A. (1996). Theta phase precession in hippocampal neuronal populations and the compression of temporal sequences.

Hippocampus *6*, 149-172.
7. Solstad, T., Boccara, C.N., Kropff, E., Moser, M.B., and Moser, E.I. (2008). Representation of geometric borders in the entorhinal cortex. Science *322*, 1865-1868.
8. Wilson, M.A., and McNaughton, B.L. (1993). Dynamics of the hippocampal ensemble code for space. Science *261*, 1055-1058.
9. Zhang, S.J., Ye, J., Miao, C., Tsao, A., Cerniauskas, I., Ledergerber, D., Moser, M.B., and Moser, E.I. (2013). Optogenetic dissection of entorhinal-hippocampal functional connectivity. Science *340*, 1232627.

Acknowledgments: We are indebted to H. Wu, H. Chen, W. Tang, Q. Ren, C. Zhang, H. Yang and J. Ni for their encouragement and help. We thank B. Deng, L. Hu and J. Cai for their excellent technical assistance.

Funding: We are grateful for the generous startup funds from Xinqiao Hospital and Army Medical University, China. This work is also supported by a grant from the National Natural Science Foundation of China.

Author Contributions: S.-J.Z conceived the idea, designed the study and conceptualized the project. X.L. and S.-J.Z performed the experiments, collected the data and planned the analyses. X.L. made all figures. S.-J.Z. wrote the manuscript.

Competing Interests: The authors declare no competing financial interests.

Data and Materials Availability: All data and materials are available by request, and any reasonable request for data and materials should be directed to the corresponding author.

Correspondence and requests for data and materials should be addressed to:

sheng-jia.zhang@tmmu.edu.cn or sheng-jia.zhang@outlook.com